공학석사학위논문

종방향 스트립이 낮은 레이놀즈 수 익형에 미치는 영향

Aerodynamic Effects of Longitudinal Strips on a Low Reynolds Number Airfoil

2013 년 8 월

서울대학교 대학원

기계항공공학부

정 민 욱

종방향 스트립이 낮은 레이놀즈 수 익형에 미치는 영향

Aerodynamic Effects of Longitudinal Strips On a Low Reynolds Number Airfoil

지도교수 최 해 천

이 논문을 공학석사 학위논문으로 제출함

2013 년 8 월

서울대학교 대학원

기계항공공학부

정 민 욱

정민욱의 공학석사 학위논문을 인준함

2013 년 8 월

위 원 장 _____

부위원장 _____

위 원 _____

Aerodynamic Effects of Longitudinal Strips on a Low Reynolds Number Airfoil

Minuk Jung
School of Mechanical and Aerospace Engineering
Seoul National University

Abstract

In the present study, we investigate the aerodynamic effects of longitudinal strips on a two-dimensional, low Reynolds number airfoil (SD7003). The experiment is conducted in a wind tunnel at $Re_c = 0.6 \times 10^5$ and 1.0×10^5, based on the free-stream velocity U_∞ and the chord length c. By varying the width (w), height (h), and spacing (s) of the longitudinal strips, we measure the lift, drag and velocity field near the airfoil surface. The longitudinal strips delay the stall by up to 3° in the ranges of $0.02 \leq s/c \leq 0.10$ and $0.02 \leq w/c \leq 0.06$. Delayed stall causes an increase in lift and decrease in drag, resulting in a significant increase of the lift-to-drag ratio, as compared to the airfoil without strips. Velocity measurements at $AOA = 11.4°$ showed that separated flows reattach on the airfoil surface at the leading edge due to streamwise vortices.

Keywords: Longitudinal Strip, Airfoil, Stall, Lift-to-drag ratio, Reattachment, Streamwise vortex

Student number: 2011-24069

Contents

List of Figures

Figure

Nomenclature

Roman Symbols

b	airfoil span
c	airfoil chord length
D	drag force
E	energy
f	frequency
C_D	drag coefficient
C_L	lift coefficient
h	height of longitudinal strips
L	lift force
L/D	lift-to-drag ratio
Re_c	Reynolds number based on the airfoil chord, $Re_c = U_\infty c/\nu$
s	spacing between longitudinal strips
u, v	streamwise, normal velocity components, respectively
U_∞	freestream velocity
w	width of longitudinal strips
x, y, z	Cartesian coordinate (streamwise, normal, spanwise direction, respectively)

Greek Symbols

ν	kinematic viscosity
ρ	density

ω_x	streamwise vorticity

Superscripts

$(\,)'$	fluctuating components
$\overline{(\,)}$	mean quantities

Subscripts

$(\,)_\infty$	freestream

Abbreviations

AOA	angle of attack
AR	aspect ratio
APG	adverse pressure gradient
HWA	hot-wire anemometry
LSB	laminar separation bubble
PIV	particle image velocimetry
rms	root-mean-square
UAV	unmanned aerial vehicle

Chapter 1

Introduction

Recently, small unmanned aerial vehicles (UAVs) receive much attention in the military and industry. Many missions are performed with these vehicles, including military and scientific sampling, communication relay links, and surveillance. Mueller & DeLaurier (2003) suggested that vehicles which have speeds between $20 \sim 100\,km/h$ with wing spans less than $\sim 6\,m$ and masses less than $\sim 25\,kg$ could be considered as small UAVs. This low velocities and small length scales make small UAVs operate in the range of Reynolds numbers of $10^4 \sim 10^6$, small compared with the range of conventional commercial and military planes (Lissaman (1983)).

In this range of Reynolds numbers, generally called **low Reynolds number**, some complicated phenomena occur within a boundary layer. A laminar boundary layer easily separates in an adverse pressure gradient (APG) and the separated flow forms a free-shear layer which is highly unstable. Then transition to turbulence takes place, and the flow reattaches to the surface if the increased momentum overcomes the APG. This forms a laminar separation bubble (LSB, see figure 1.1), the distinctive flow structure commonly observed at low Reynolds numbers (Horton (1968); O'Meara & Mueller (1987)). The LSB, which is sensitive to the flow environment, significantly changes the flow characteristics (i.e. the lift, the drag and the pressure distribution) and sometimes it yields hysteresis effects (figure 1.2). Hence, the results of a low Reynolds number airfoil

show the wide variation with the surface roughness, the surface curvature, the freestream turbulence and other flow conditions (Gad-el-Hak (1990); Marchman (1987)).

This implies the aerodynamic performance of the airfoil could be dramatically deteriorated by the subtle change of conditions. Therefore, the control of a low Reynolds number airfoil is important to get better performance of small UAVs. For a comprehensive review on this topic, see Gad-el-Hak (1990). Among many flow control methods, turbulators are commonly used as passive control devices. A turbulator is a device that promotes the transition, which leads to the early reattachment and attenuation of the main separation. Selig *et al.* (1989) applied transition ramps and boundary-layer trips on various kinds of airfoil at low Reynolds numbers and achieved large drag reductions. Meanwhile, Kerho *et al.* (1993) applied vortex generators in order to decrease the airfoil drag by controlling LSBs. In the form of serrations, ridges, surface roughness are also used as turbulators (Gad-el-Hak (1990)).

Longitudinal strips could also be used as turbulators. A similar surface configuration is observed in nature, rib structure of the scallop shell surface (figure 1.3). Sea scallops exhibit an exceptional swimming performance while escaping from a slow predator such as a starfish (Manuel, J. L. & Dadswell, M. J. (1993)). Bushnell *et al.* (1991) conjectured that ribs on a scallop shell control flow separation through vortex generation. Choi *et al.* (2012) conducted a wind tunnel experiment at $Re = 10^5$ and showed that ribs enhance the lift-to-drag ratio of the scallop. This means that the scallop-ribs-like device could be used to enhance the aerodynamic performance on a low Reynolds airfoil. However, to the author's knowledge, although there have been some studies related to spanwise wavy surface wings (Zverkov *et al.* (2008); Lin *et al.* (2013)), no precedent study has been conducted which discussed the effects of longitu-

dinal strips on an airfoil. Therefore, a study on longitudinal strips is needed to explain the mechanism and enhance the aerodynamic performance of a low Reynolds number airfoil.

In the present study, effects of longitudinal strips on a low Reynolds number airfoil are investigated. First, drag and lift forces are directly measured on a two-dimensional airfoil with and without longitudinal strips to verify the effects of strips. Then a parametric study is conducted to optimize the longitudinal strips. Finally, velocity measurements around the airfoil using hot-wire anemometry (HWA) and particle image velocimetry (PIV) are performed to understand the detailed flow characteristics.

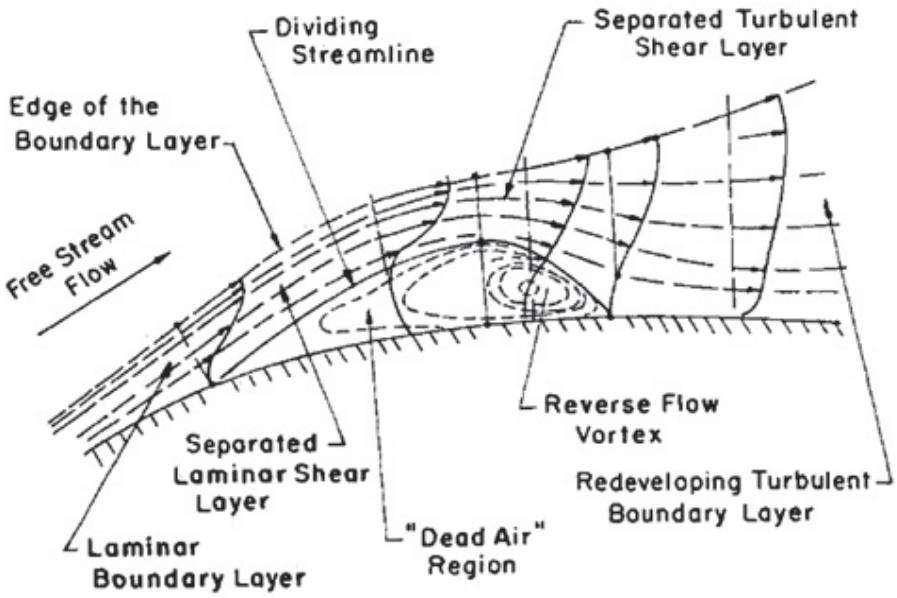

Figure 1.1. Schematic diagram of a laminar separation bubble, Horton (1968).

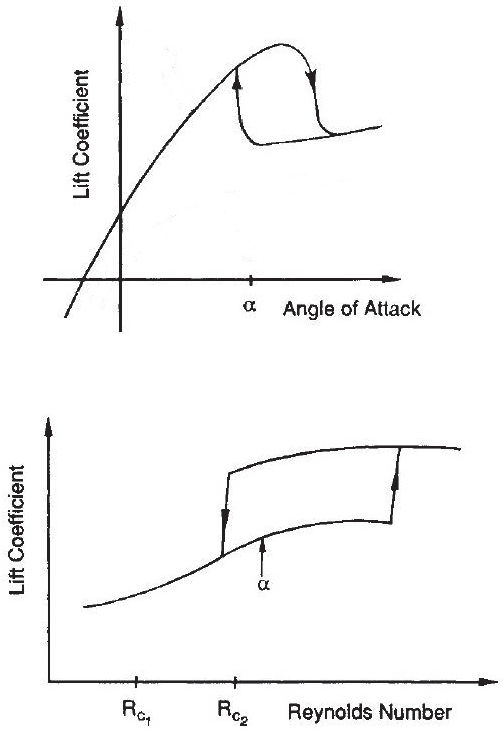

Figure 1.2. Illustration of hysteresis effects, Gad-el-Hak (1990).

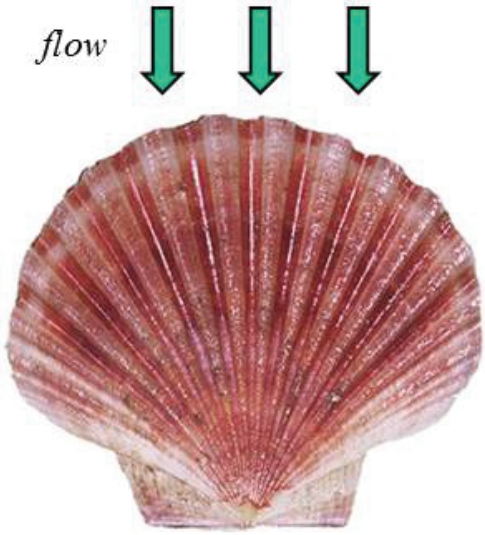

Figure 1.3. Surface of the scallop, *Pecten fumatus* (Photo supplied by Fisheries research & development corporation, Australia).

Chapter 2

Experimental Setup

2.1 Wind tunnel and model

Figure 2.1 shows the schematic diagram of the present experimental setup. The experiment is conducted in an open-circuit blowing-type wind tunnel. The test section made of acryl is measured $3\,m \times 0.6\,m \times 0.3\,m$ in streamwise (x), vertical (y), spanwise (z) direction, respectively. The maximum wind speed of the test section is $30\,m/s$ and the uniformities of mean velocity and freestream turbulence intensity are both within $0.5\,\%$ at $12 m/s$ (Park & Choi (2010)). The Reynolds numbers for the present experiment based on the chord length and freestream velocity U_∞ of 7.5 and $12.5\,m/s$ are $Re_c = 0.6 \times 10^5$ and 1.0×10^5.

In this study, SD7003 airfoil (figure 2.4) is selected for the two-dimensional airfoil model. SD7003 has a maximum thickness of $8.5\,\%$ and a maximum camber of $1.48\,\%$ of the chord length (Selig *et al.* (1995)). Because SD7003 was designed to have a gradual upper-surface pressure recovery (Selig *et al.* (1989)), it shows a long, stable LSB over a wide range of angles of attack (AOA) below $Re_c = 10^5$ (Ol *et al.* (2005)). Due to this superior behavior, there have been many numerical (Galbraith & Visbal (2010); Shyy *et al.* (2007); Zhou & Wang (2012)), and experimental studies (Burgmann *et al.* (2008); Radespiel *et al.* (2006)) on SD7003. The airfoil made of ABS resin with a chord of $c = 0.12\,m$ and a span of $b = 0.24\,m$ is tested between two endplates. Boutilier *et al.*

(2012) reported that lift coefficient curves and surface-pressure distributions are converged if the aspect ratio of a two dimensional airfoil is larger than 2.0, which is the aspect ratio of present study.

Endplates made of acyrl are mounted to get two-dimensionality. The endplates are set up with the distance of $23 \sim 24\,mm$ from each side wall of the test section, which sufficiently contain the boundary layer of each side wall. The gap between the airfoil and endplates are less than $1\,mm$, satisfying the value suggested by Barlow *et al.* (1999) and Mueller & Burns (1982). According to Barlow *et al.* (1999), the gap should be less than 0.5 % of the span, which is equivalent to $\sim 1.2\,mm$ in the present setting. Moreover, Mueller & Burns (1982) showed that the gap size between 0.1 and $1.4\,mm$ are usually acceptable and do not affect the results. Figure 2.1 (b) shows the schematics of the test section.

2.2 Force measurement

An in-house two-component force balance unit that consists of two 1-axis loadcells (CAS BCL-1L in the streamwise direction, CAS BCL-3L in the normal direction) is used to measure the lift and drag forces on the airfoil simultaneously. The interference by other components of force in each loadcell is measured less than 2 % and taken into account in calculating the lift and drag coefficients from the loadcell output voltages. This unit is connected to the airfoil through a strut, covered by a shroud isolating the strut from the freestream. Forces are measured with varying the AOA in the range of $0^\circ \leq AOA \leq 16^\circ$ by increments of $0.5^\circ \sim 1.5^\circ$. The AOA is controlled by a rotating stage (manual) which has a resolution of $1.4'$. To check the existence of hysteresis effects, measurements are performed with both increasing and decreasing the AOA. In the present study,

no hysteresis effect is observed for all tests, and the error between two cases is within $\pm 1.5\,\%$. The signals from the loadcells are amplified by a signal conditioning amplifier (Scale-Tron STT-200S) and digitized by an A/D converter (NI PXI-6259). The data are sampled over $30\,s$ with a sampling rate of $10\,kHz$ to obtain a fully converged mean and post-processed after the sampling with the LABVIEW software.

The lift (C_L), drag (C_D) coefficients are defined as follows:

$$C_L = L \,/\, 0.5\rho {U^2}_\infty \, bc\,, \tag{2.1}$$

$$C_D = D \,/\, 0.5\rho {U^2}_\infty \, bc\,, \tag{2.2}$$

where ρ is air density, bc is the total planform area of the airfoil, and L, D are the lift and drag forces, respectively. The freestream velocity, U_∞ is measured directly using a manometer (MKS220DD). The resolution of the manometer is $0.001\,\%$ at full scale of 10 Torr and the signal is sampled simultaneously with force measurement. Wind tunnel corrections (Barlow *et al.* (1999)) are applied to the measured lift and drag coefficients.

2.3 Velocity measurement

The velocity profiles around the airfoil are measured with an I-type hot-wire probe and an in-house hot-wire anemometer. A wire that consists of platinum-$10\,\%$ rhodium with a diameter of $1.5\,\mu m$ and a length of $0.5\,mm$ is soldered to the prongs of the probe. At an overheat ratio of 1.2, the cutoff frequency of the anemometer is approximately $30\,kHz$. The voltages from the anemometer are calibrated at the freestream with a manometer. A fourth order polynomial with at least seven calibration points is used to form a least-square fit of the

voltage versus the velocity. The uncertainty in the velocity calibration is within 0.5 %. The output from the hot-wire probe is sampled for 16 s at the rate of 32 kHz. The hot-wire probe is mounted on a three-dimensional traversing unit of 0.02 mm resolution. This unit is controlled automatically, using the LABVIEW software and a stepping motor. When the hot-wire breaks due to the contact of the probe on the airfoil surface, this point is set as a origin along the normal direction. Thus the minimum distance of the point closest to the surface is 0.02 mm.

For a further investigation of the velocity around the airfoil, a y-z plane PIV at the suction side of the airfoil is conducted. Figure 2.3 shows the schematic diagram of the PIV system. The present PIV system consists of an Nd-Yag laser (NEW WAVE RESEARCH Solo 120), a delay generator, a fog generator (SAFEX F2010), optical lens (Nikon) and a CCD camera (VH). A Nd-Yag laser is used as the light source and the SAFEX standard fog fluid is used as seeding particles. The fog fluid is transformed into smoke by the fog generator. As described in figure 2.3, the laser is installed at one side of the wind tunnel and a sheet of the laser makes a y-z plane. To prevent the reflection of the laser, the lusterless black paint is coated on the airfoil surface. The CCD camera is located behind the test section to view a y-z plane. The CCD camera captures the field of views whose size are $(30 \pm \epsilon)\, mm \times (60 \pm \epsilon)\, mm$ in vertical (y), spanwise (z) direction, respectively. The initial size of a interrogation window is 64×64 and recursively processed into 32×32 with 50 % overlapped images. The spatial resolution is $(0.3 \pm \epsilon) mm$ which corresponds to about 0.25 % of the chord length. Here, ϵ means a changeable value due to errors from the experimental setting. $4,000$ vector fields are averaged to analyze mean quantities from velocity profile.

2.4 Parameters of strips

Three parameters are chosen to investigate the effect of longitudinal strips. As shown in figure 2.4 (a), width (w), height (h) of strips and spacing (s) between strips are the parameters that determine the longitudinal strips. For convenience, strips made of Kent paper are attached uniformly from the leading edge of the airfoil to the trailing edge on both the suction and pressure side.

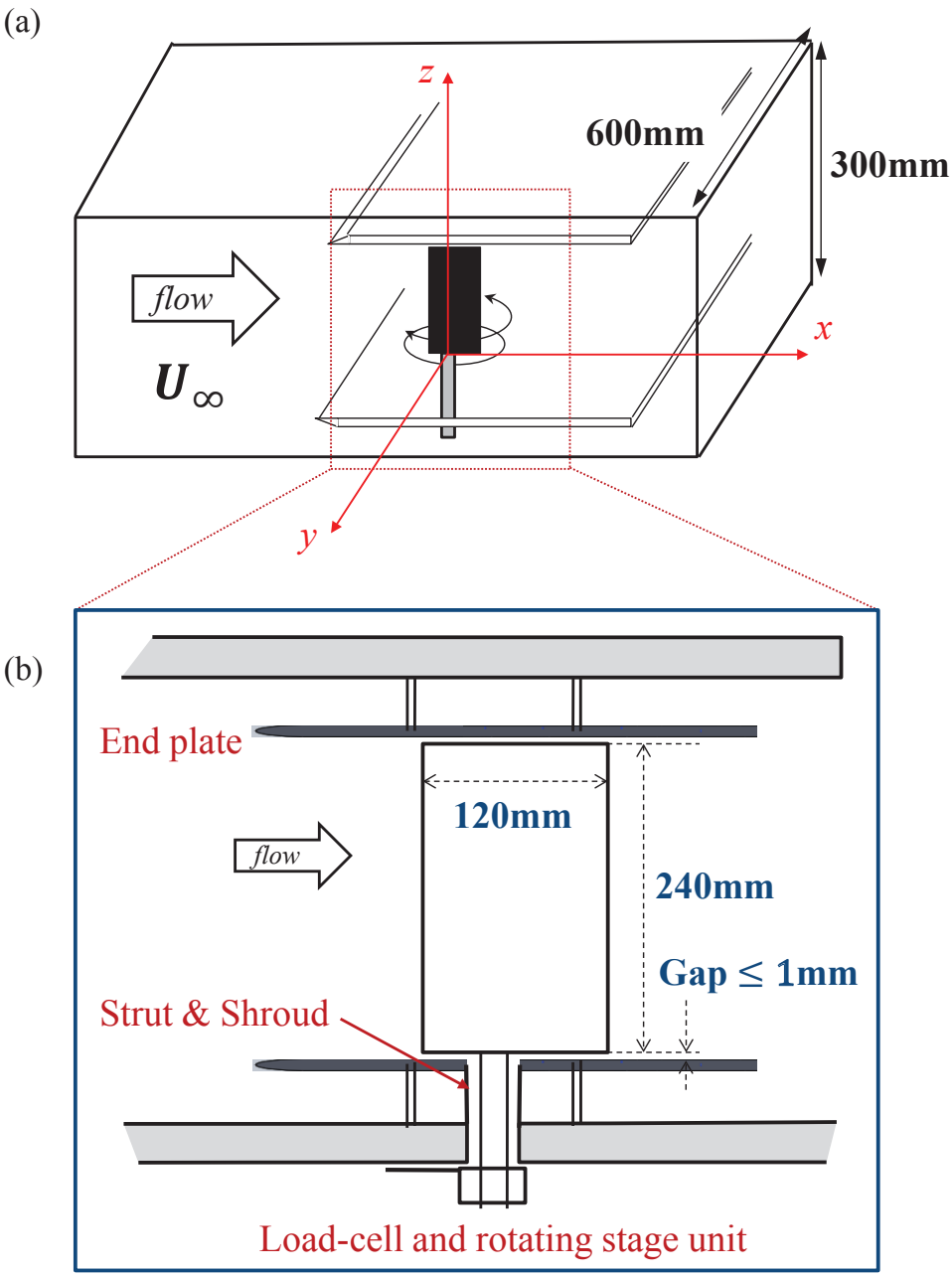

Figure 2.1. Schematic diagram of the wind tunnel test section.

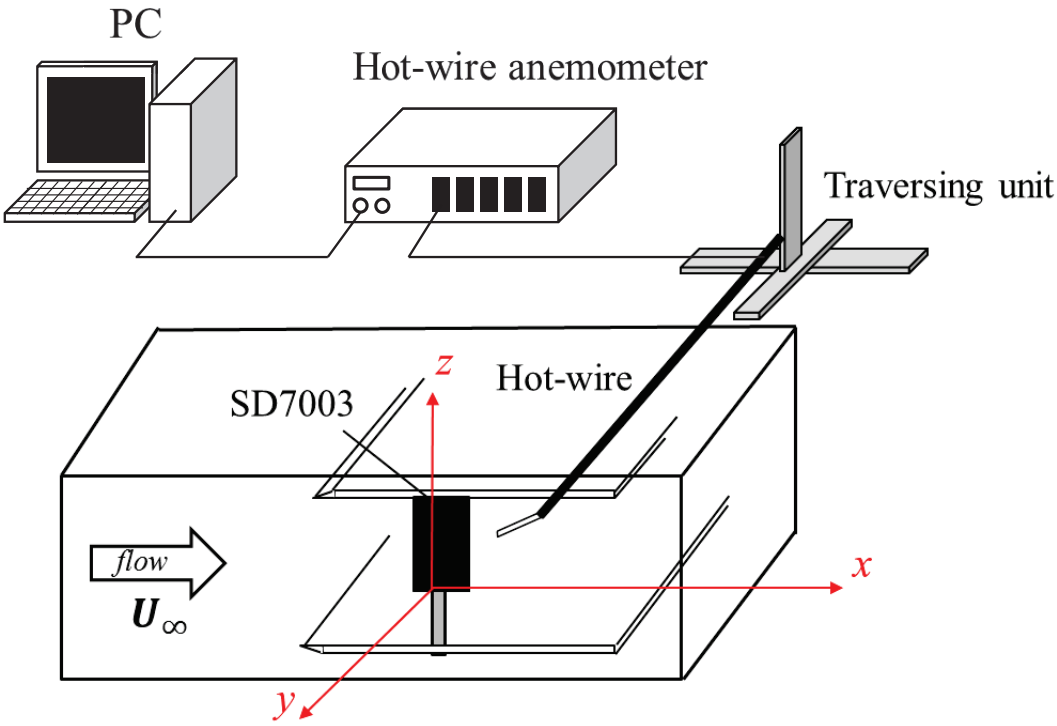

Figure 2.2. Schematic diagram of the HWA measurement.

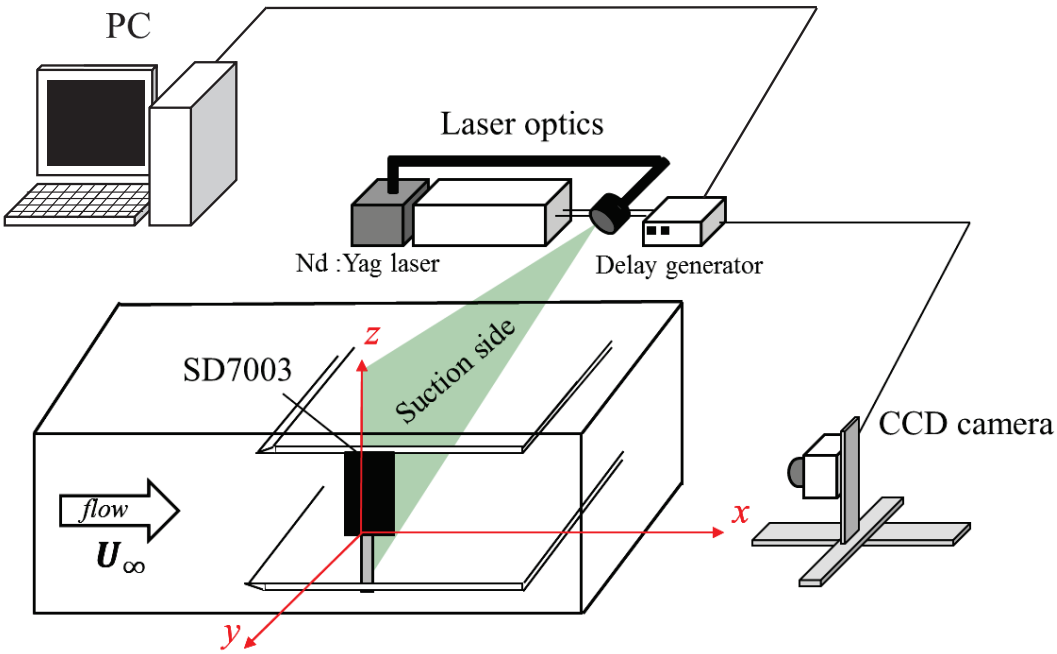

Figure 2.3. Schematic diagram of the PIV measurement.

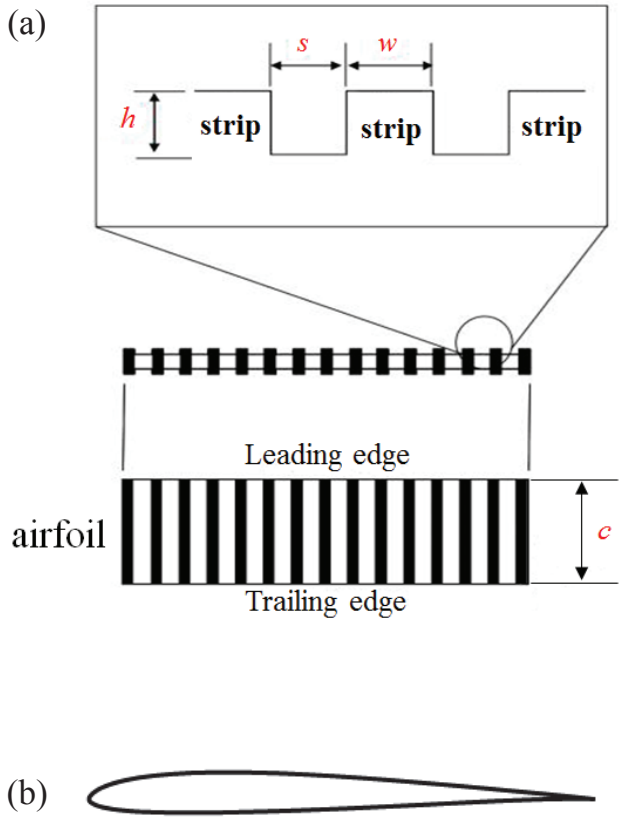

Figure 2.4. (a) parameters for longitudinal strips; (b) a cross section of the SD7003 airfoil.

Chapter 3

Parametric Study

3.1 Effects of height (h)

Figure 3.1 and 3.2 show the variations of lift (C_L) and drag (C_D) coefficients with the AOA for two heights of strips, $h/c = 0.003$ and 0.006. The width and spacing are fixed to $w/c = 0.02, s/c = 0.06$. After the stall angle ($\sim 10°$) of the airfoil without strips (baseline airfoil), an increase in the lift coefficient and decrease in the drag coefficient are observed at both $h/c = 0.003$ and 0.006. Regardless of Reynolds numbers, similar trends are shown if the parameters are same. However, at $h/c = 0.006$, the lift decreases and the drag increases before the baseline stall angle. It might be due to the large height relative to the airfoil thickness t, which is $h/t \sim 0.07$. On the other hand, at $h/c = 0.003$, the lift and drag before the baseline stall angle are similar to that without strips. Moreover, the airfoil with $h/c = 0.003$ strips shows higher lift and lower drag than the airfoil with $h/c = 0.006$ in the whole range of the AOA. Because of this reason, all the other experiments are conducted at the height of $h/c = 0.003$.

3.2 Effects of spacing (s) and width (w)

Figure 3.3 and 3.4 show the variations of the lift (C_L) and drag (C_D) coefficients with the AOA for various spacings. The width are fixed to $w/c = 0.02$ and spacings are varied from 0.02 to 0.10. In these figures, stall delay is observed

at all spacings and Reynolds numbers. This is the cause of the lift enhancement and drag reduction after the stall of the baseline. At low Reynolds numbers, the drag increases drastically right after the stall (Selig *et al.* (1989); Selig *et al.* (1995)). Therefore, a large amount of decrease in drag is obtained when stall delay occurs, as shown in the figure 3.4. Besides, the amount of increase in the lift is also large and the lift curve shows a plateau shape instead of a sharp peak at the high AOA. But the lift and drag show no significant difference for the range of spacing considered. Among the spacings, $s/c = 0.06$ is chosen for investigating the effects of width. Figure 3.5 and 3.6 show the variations of the lift (C_L) and drag (C_D) coefficients with the AOA for various widths. The graphs show similar characteristics to that obtained from the parametric study of the spacing. For the range of width considered, the strips increase the lift and decrease the drag to the similar extent. Stall delay is about 3° at $w/c = 0.03$ and the others.

3.3 Lift-to-drag ratio

The maximum range or endurance at a given cruise speed is the goal of designing small UAVs. According to Brequet, the maximum range of propeller-driven aircraft is expressed as follows:

$$Range = \frac{\eta}{c}\frac{L}{D}\ln\frac{W_0}{W_1}, \tag{3.1}$$

where η is the propeller efficiency, c is the specific fuel consumption, W_0 is the gross weight, W_1 is the weight of the aircraft without fuel and L/D are the lift-to-drag ratio. Thus, to extend the range to the maximum, the lift-to-drag ratio at the cruise condition should be maximized. Due to this relation, the lift-

to-drag ratio is generally used as a criterion for the aerodynamic performance. Figure 3.7 shows the variation of the lift-to-drag ratio with the AOA. At low AOA, the airfoil with strips shows no significant difference from the airfoil without strips. However, a significant increase of lift-to-drag ratios is observed near the stall. Maximum increase in the lift-to-drag ratio is occurred at $AOA \simeq 11°$ for all model. At the parameters of $w/c = 0.03$, $s/c = 0.06$, $h/c = 0.003$, the maximum increase of the lift-to-drag ratio is about 100 % at $AOA = 11.4°$. To analyze the effects, velocity measurement are conducted at $Re_c = 0.6 \times 10^5$, $AOA = 11.4°$ with strips of these parameters.

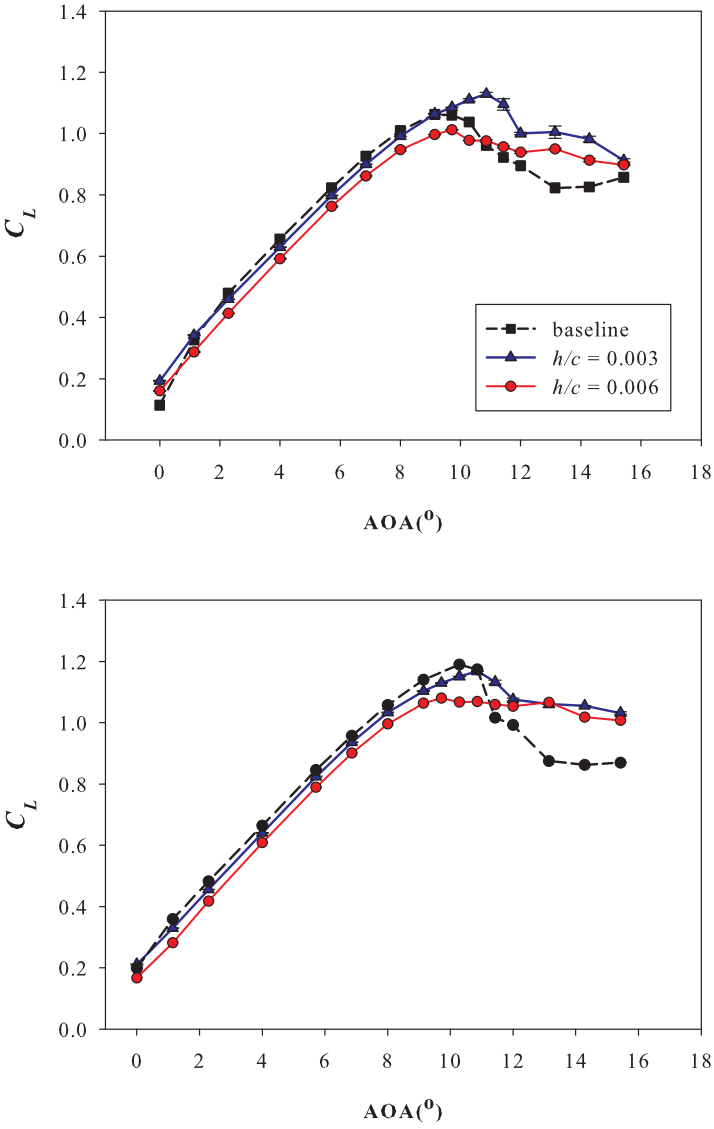

Figure 3.1. Effects of strip height (h) on lift coefficients: (a) $Re_c = 0.6 \times 10^5$; (b) $Re_c = 1.0 \times 10^5$.

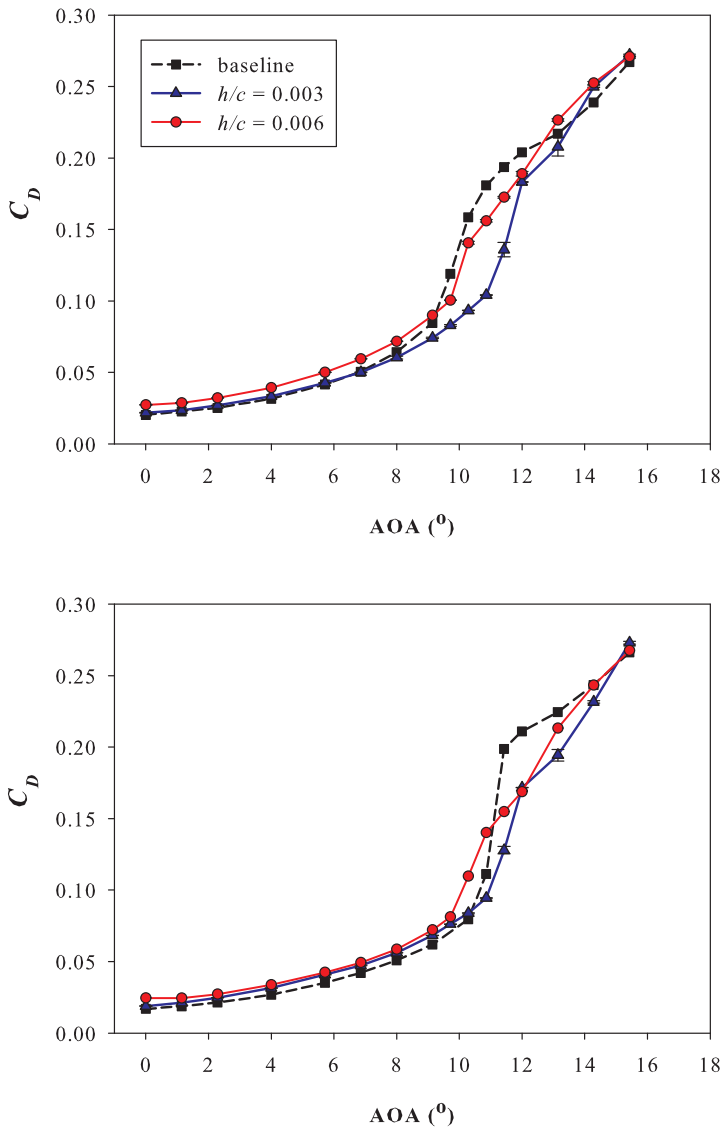

Figure 3.2. Effects of strip height (h) on drag coefficients: (a) $Re_c = 0.6 \times 10^5$; (b) $Re_c = 1.0 \times 10^5$.

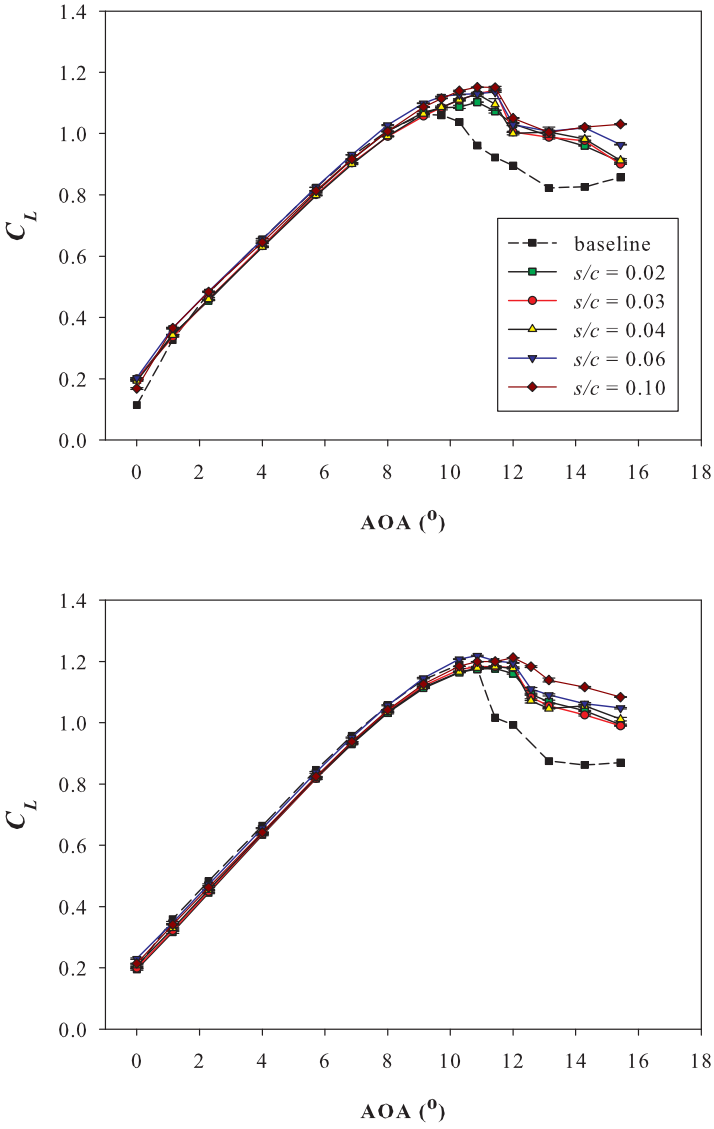

Figure 3.3. Effects of strip spacing (s) on lift coefficients: (a) $Re_c = 0.6 \times 10^5$; (b) $Re_c = 1.0 \times 10^5$.

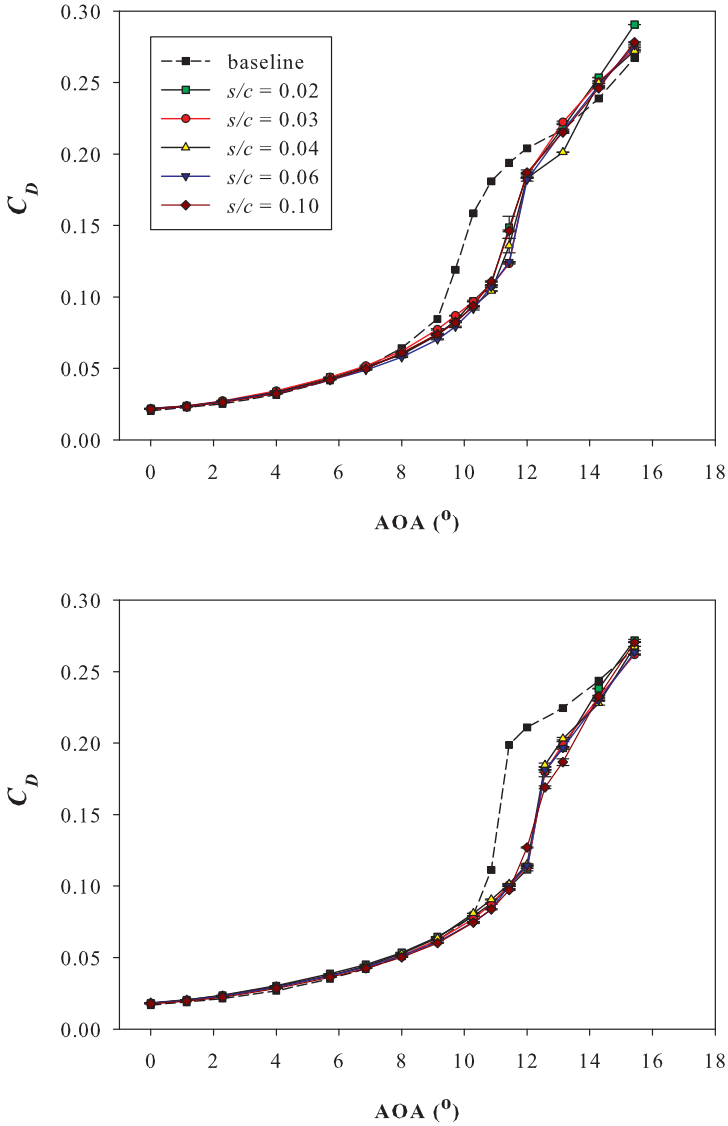

Figure 3.4. Effects of strip spacing (s) on drag coefficients: (a) $Re_c = 0.6 \times 10^5$; (b) $Re_c = 1.0 \times 10^5$.

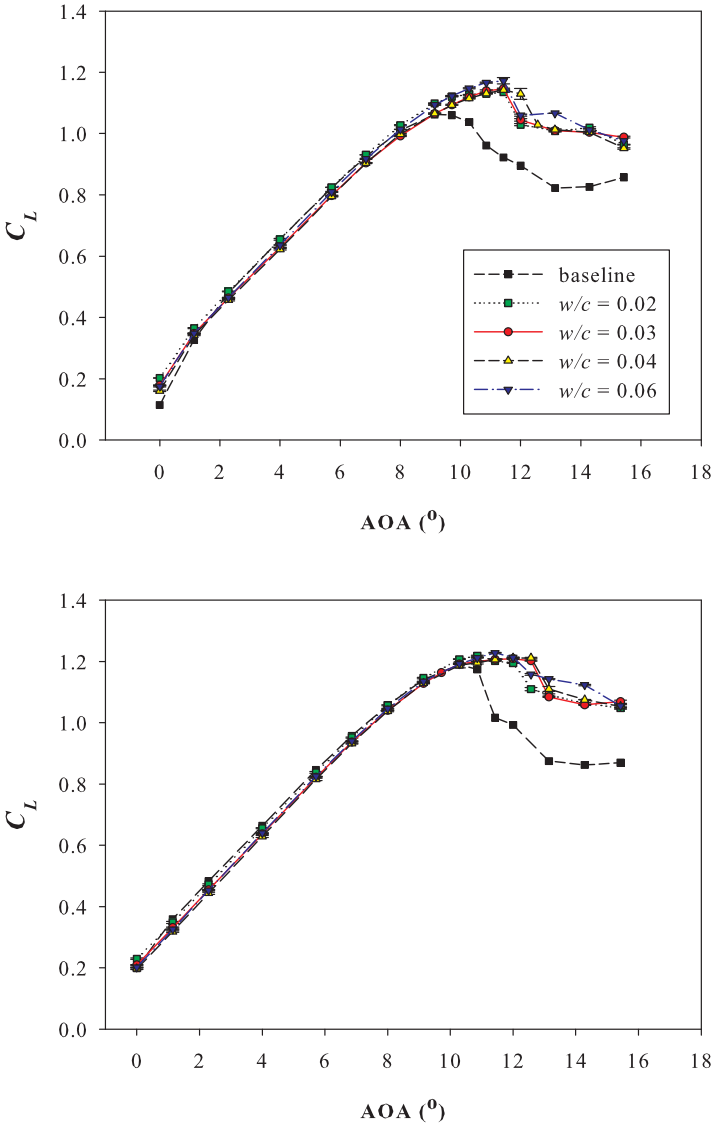

Figure 3.5. Effects of strip width (w) on lift coefficients: (a) $Re_c = 0.6 \times 10^5$; (b) $Re_c = 1.0 \times 10^5$.

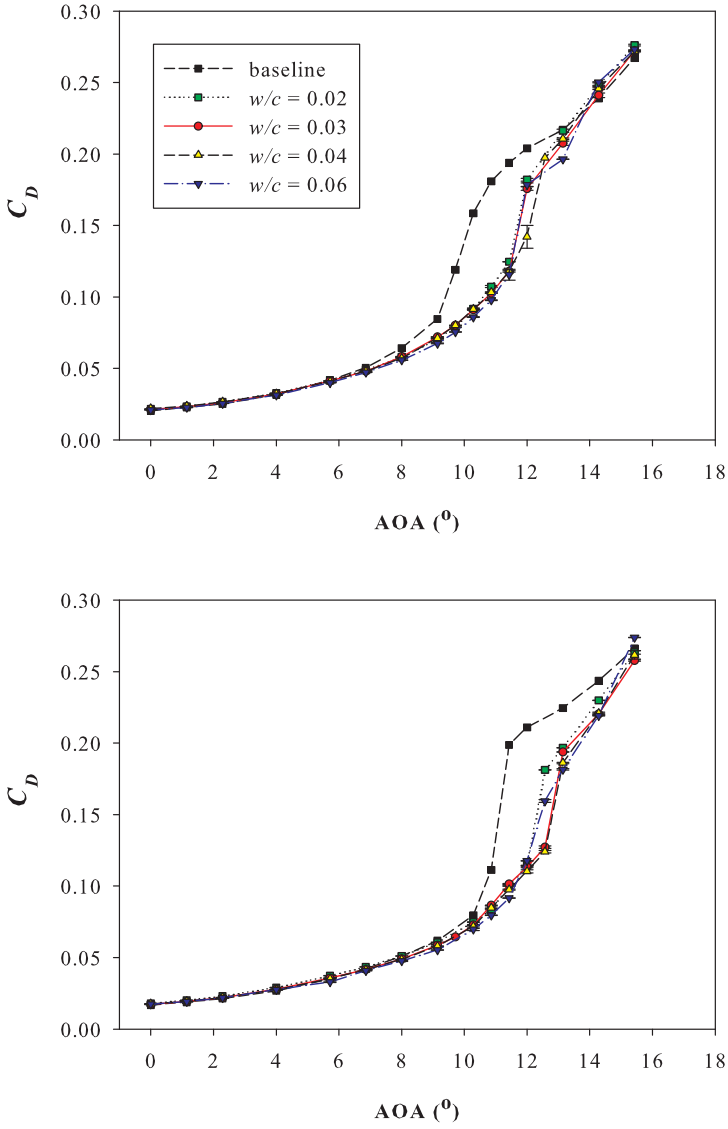

Figure 3.6. Effects of strip width (w) on drag coefficients: (a) $Re_c = 0.6 \times 10^5$; (b) $Re_c = 1.0 \times 10^5$.

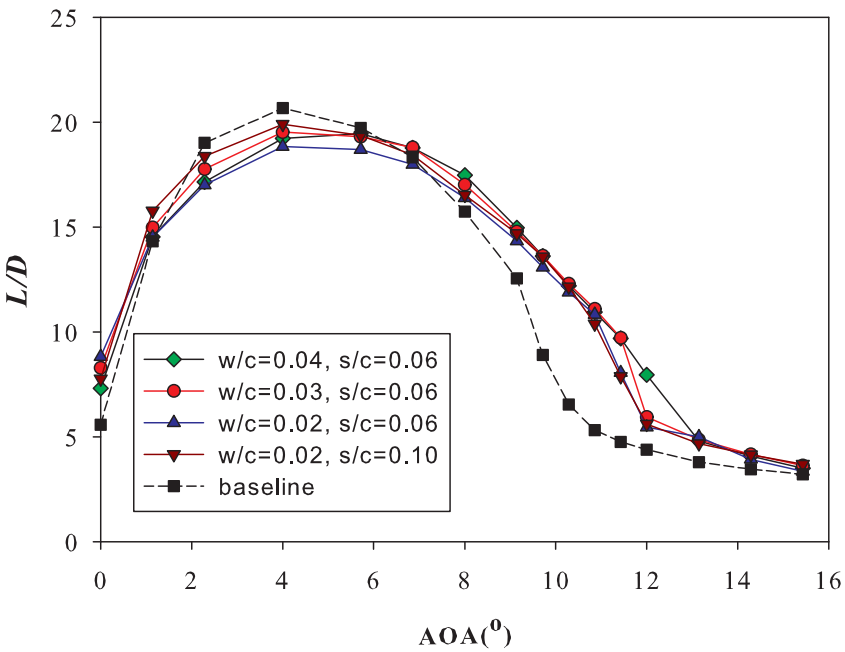

Figure 3.7. Lift-to-drag ratios for selected parameters at $Re_c = 0.6 \times 10^5$.

Chapter 4

Flow Visualization

4.1 Streamwise velocity measurement

Two flow visualization methods, HWA and PIV are conducted at $Re_c = 0.6 \times 10^5$ and $AOA = 11.4°$ to analyze the enhancement of the aerodynamic performance. As mentioned before, the parameters chosen are $w/c = 0.03$, $s/c = 0.06$ and $h/c = 0.003$. First, streamwise velocities are measured with HWA. Figure 4.1 and 4.2 show the velocity profiles above the suction side of the airfoil. Note that, owing to the usage of a I-type single hot-wire probe, the measured velocity does not represent the actual streamwise velocity component. Moreover, near and after a flow separation or inside a separation bubble where reversed flows occur, the measured mean velocity and rms velocity fluctuation profiles do not indicate the real flow statistics. Nevertheless, the variation of measured velocity along the normal (y) and streamwise (x) directions clearly provides how the flow characteristics change quantitatively. The streamwise velocity signals at the y locations where the maximum u'_{rms} is obtained is transformed to obtain their energy spectra. Energy spectra are calculated using a fast Fourier transform of the averaged and windowed signals (see Choi & Moin (1990) for details). The energy spectra is defined as follows:

$$E(\omega) = \hat{f}\hat{f}^*, \quad f = \frac{1}{\sqrt{2\pi}} \int_{-\infty}^{\infty} u(t) e^{-i\omega t}\, dt. \tag{4.1}$$

Figure 4.3 shows these energy spectra at various streamwise positions.

Figure 4.1 shows the velocity profiles at 20, 50 and 90 % of the chord in the streamwise direction. There are two velocity profiles around the airfoil with strips, one above the strip and the other above the airfoil. The velocity profiles with and without strips show the difference. Without strips, the mean velocity profile is almost constant along the y direction near the airfoil surface, and the level of rms velocity fluctuation is larger than that with strips. Because the constant near-wall mean velocity profile along the y direction infers the existence of a flow separation when a I-type probe is used, we can conclude that the flow is separated on the surface of the baseline. On the other hand, the mean velocity profiles with strips show sharp gradients along the y direction, which imply the attached flows. Spanwise variation on the airfoil with strips is negligible. To investigate the detailed flow characteristics, streamwise velocities near the leading edge (LE) are measured.

Figure 4.2 shows the velocity profiles near the LE. Without strips, a separation detects already at $x/c = 0.05$ and separation region grows larger as flow moves downstream. The maximum rms velocity fluctuation moves outward along the y direction as flows go downstream, which coincides with the separation growth. With strips, flows also separate from the airfoil before $x/c = 0.05$ (above the airfoil) or after $x/c = 0.05$ (above the strips). However, flows above both reattach to the airfoil before $x/c = 0.20$, although flows on the airfoil with strips shows spanwise variation between $x/c = 0.05$ and $x/c = 0.20$. The flows form the LSB, instead of the separation in the whole range. From the view point of stall, the flow reattachment instead of the separation retards the AOA where a stall begins. That is to say, the flow reattachment causes the stall delay.

Energy spectra explains the reason for the flow reattachment. At $x/c = 0.05$, two peaks at high frequencies are observed in energy spectra above the airfoil

with strips, while the other two show low energy levels at high frequencies (figure 4.3 (a)). Then at $x/c = 0.10$, energies grow at high frequencies on the airfoil with strips, forming broadband spectra. Finally, after $x/c = 0.15$, turbulence characteristics are observed on the airfoil with strips. Although the rms velocity fluctuations decay as flows go downstream (figure 4.2 (b)), flows rapidly transit into turbulence between $x/c = 0.05$ and 0.15. The $-5/3$ slope of Kolmogorov spectrum is plotted together at figure 4.3 (c) and (d). On the other hand, the energy on the baseline shows slower growth at high frequencies even though the rms velocity fluctuation is higher than that of the airfoil with strips. Therefore, disturbances generated by the strips accelerate the transition to turbulence and this makes the flow reattach to the surface.

4.2 Velocity field on y-z plane

The y-z PIV is conducted to find how the strips disturb the flow around the airfoil. Streamwise location of $x/c = 0.05$ is chosen because the energy growth at high frequencies begins from this location. Figure 4.4 shows the instantaneous streamwise vorticity contour with velocity vectors. On the airfoil with strips, a counter rotating vortex pair is observed between two strips while no significant characteristic is observed on the baseline. The spanwise pressure gradient, the difference of boundary layers, etc. could be the source of this streamwise vortex pair. Figure 4.5 shows the rms normal velocity, v'_{rms} contour. Due to the streamwise vortices, there is a spanwise variation of v'_{rms} on the airfoil with strips. Also, the magnitude of the v'_{rms} with strips is larger than that without strips. This increase in v'_{rms} due to streamwise vortices shows up as high energy levels at high frequencies in energy spectra.

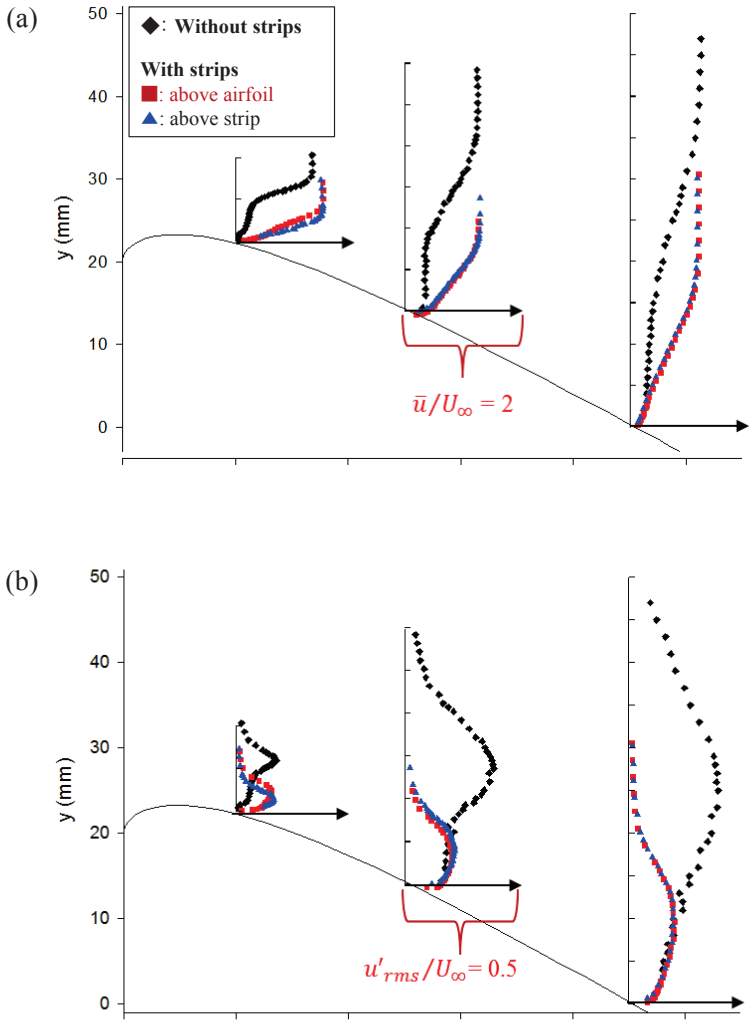

Figure 4.1. Profiles of: (a) mean streamwise velocity; (b) rms streamwise velocity at $x/c = 0.2$, 0.5 and 0.9.

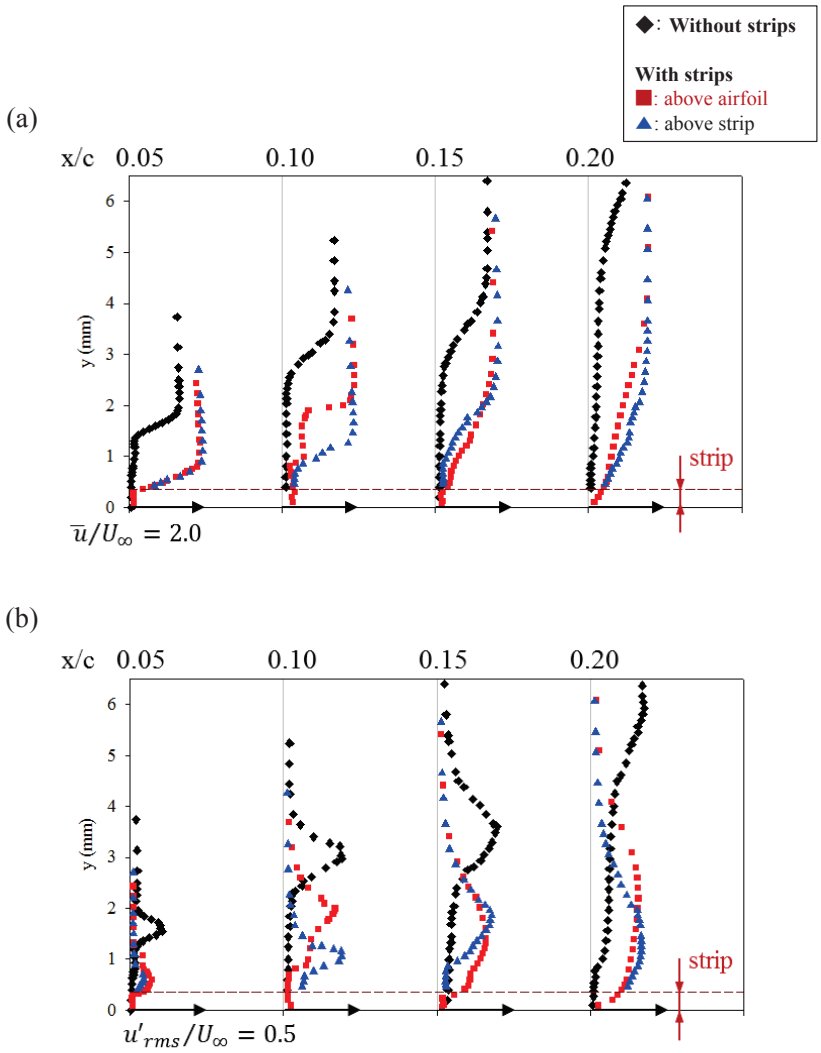

Figure 4.2. Profiles near the LE of: (a) mean streamwise velocity; (b) rms streamwise velocity.

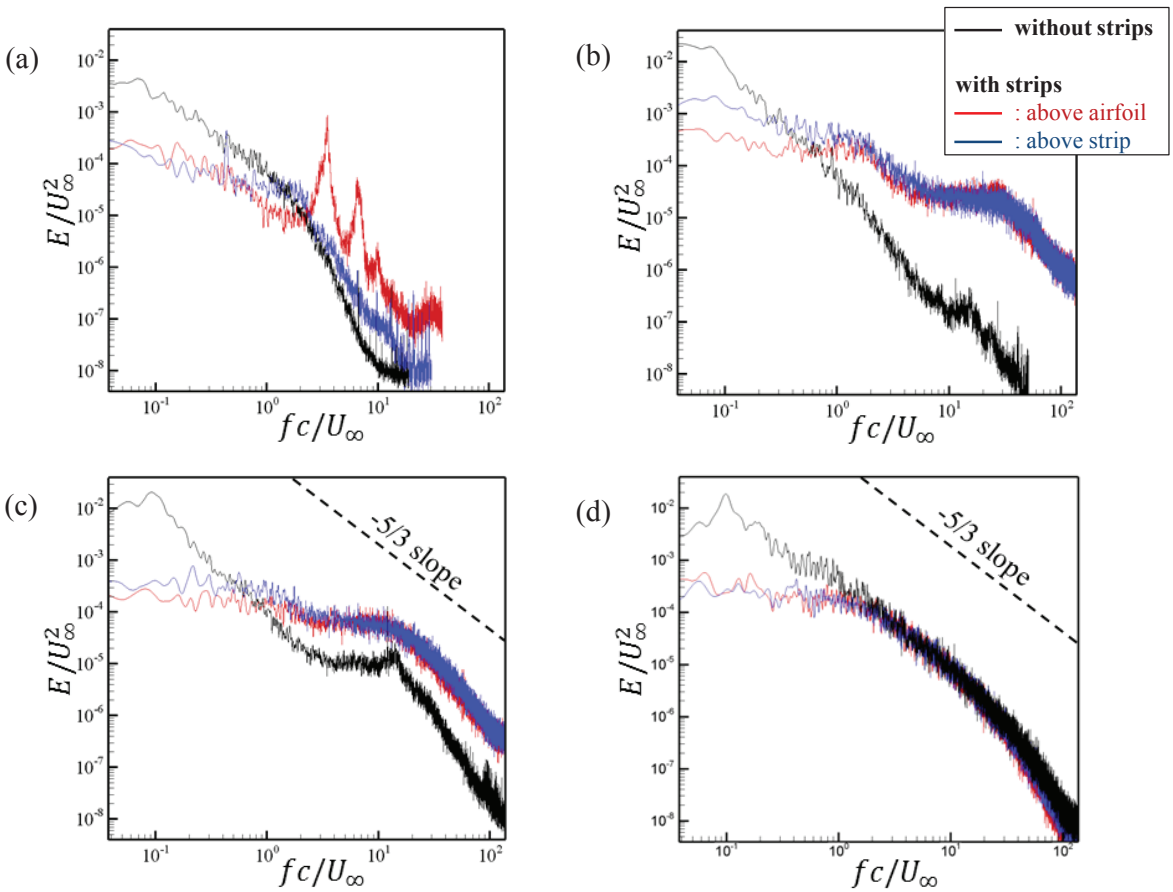

Figure 4.3. Energy spectra of the streamwise velocity at the y location having maximum u'_{rms}: (a) at $x/c = 0.05$; (b) at $x/c = 0.10$; (c) at $x/c = 0.15$; (d) at $x/c = 0.90$.

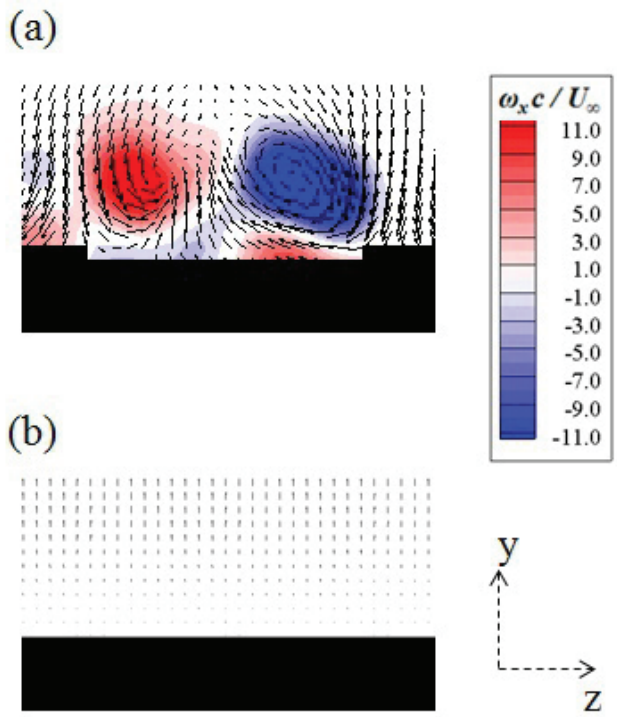

Figure 4.4. Instantaneous streamwise vorticity contours with velocity vectors on the airfoil: (a) with strips; (b) without strips.

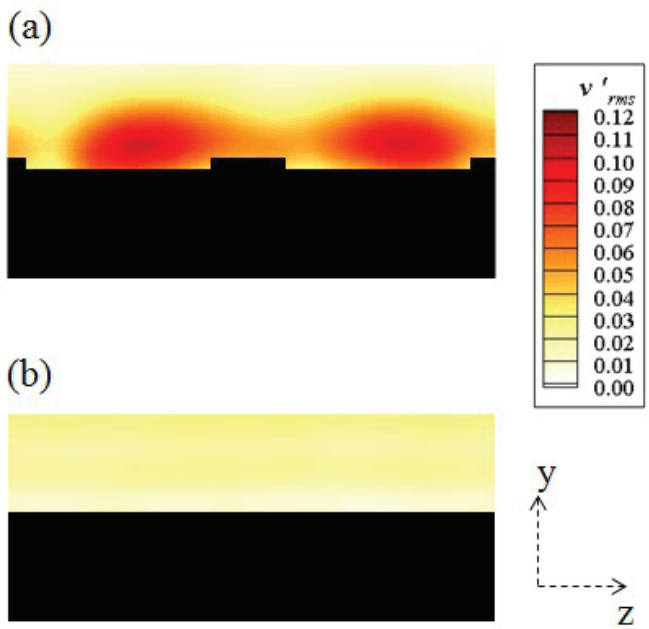

Figure 4.5. Contours of the rms normal velocity: (a) with strips; (b) without strips.

Chapter 5

Conclusion

In the present study, the effects of longitudinal strips on a low Reynolds number SD7003 airfoil was investigated at $Re = 0.6 \times 10^5$ and 1.0×10^5. The airfoil with strips showed stall delay, leading to increase in lift and decrease in drag. Parametric study is conducted to optimize the strips. The airfoil performs better at a lower height $h/c = 0.003$. However, no significant difference of the lift and drag was observed with varying the spacing and width. The lift-to-drag ratio increased considerably near and after the stall angle, about 100%. With strips, velocity measurements near the stall angle, $AOA = 11.4°$ showed that separated flows reattach on the airfoil surface at the leading edge. Streamwise vortices were observed, and this increased v'_{rms}. This accelerated the transition to turbulence, and this turbulent flow reattached to the airfoil surface. Therefore, the longitudinal strips should be an effective device to enhance the aerodynamic performance on a low Reynolds airfoil.

References

Barlow, J. B., Rae, W. H. & Pope, A. 1999 *Low-Speed Wind Tunnel Testing.* 3rd ed., Wiley.

Boutilier, M. S. H. & Yarusevych, S. 2012 Effects of end plates and blockage on low-Reynolds-number flows over airfoils. *AIAA J.* **50**, 1547–1559.

Bushnell, D. M. & Moore, K. J. 1991 Drag reduction in nature. *Annu. Rev. Fluid Mech.* **23**, 65–79.

Burgmann, S., Dannemann, J. & Schröder, W. 2008 Time-resolved and volumetric PIV measurements of a transitional separation bubble on an SD7003 airfoil. *Exp. Fluids* **44**, 609–622.

Choi, H. & Moin, P. 1990 On the space-time characteristics of wall-pressure fluctuations. *Phys. Fluids A* **2**, 1450–1460.

Choi, H., Park, H., Sagong, W. & Lee, S.-I. 2012 Biomimetic flow control based on morphological features of living creatures. *Phys. Fluids* **24**, 121302.

Gad-el-Hak, M. 1990 Control of low-speed airfoil aerodynamics. *AIAA J.* **28**, 1537–1552.

Galbraith, M. C. & Visbal, M. R. 2010 Implicit large eddy simulation of low-Reynolds-number transitional flow past the SD7003 airfoil. *AIAA Paper* 2010-4737.

Horton, H. P. 1968 *Laminar separation bubbles in two and three-dimensional incompressible flow.* PhD thesis. Univ. London.

Kerho, M., Hutcherson, S., Blackwelder, R. F. & Liebeck, R. H.

1993 Vortex generators used to control laminar separation bubbles. *J. Aircraft* **30**, 315–319.

Lin, Y. F., Lam, K., Zou, L. & Lin, Y. 2013 Numerical study of flows past airfoils with wavy surfaces. *J. Fluid Struct.* **36**, 136–148.

Lissaman, P. B. S. 1983 Low-Reynolds-number airfoils. *Annu. Rev. Fluid Mech.* **15**, 223–239.

Marchman, J. F. 1987 Aerodynamic testing at low Reynolds numbers. *J. Aircraft* **24**, 107–114.

Manuel, J. L. & Dadswell, M. J. 1993 Swimming of juvenile sea scallops, *Placopecten magellanicus*(Gmelin): a minimum size for effective swimming? *J. Exp. Mar. Biol. Ecol.* **174**, 137–175.

Mueller, T. J. & Burns, T. F. 1982 Experimental studies of the Eppler 61 airfoil at low Reynolds numbers. *AIAA paper* 82-0345.

Mueller, T. J. & DeLaurier J. D. 2003 Aerodynamics of small vehicles. *Annu. Rev. Fluid Mech.* **35**, 89–111.

Ol, M. V., Hanff, E., McAuliffe, B., Scholz, U. & Kähler, C. 2005 Comparison of laminar separation bubble measurements on a low Reynolds number airfoil in three facilities. *AIAA Paper* 2005-5149.

O'Meara, M. M. & Mueller, T. J. 1987 Laminar separation bubble characteristics on an airfoil at low Reynolds numbers. *AIAA J.* **25**, 1033–1041.

Park, H. & Choi, H. 2010 Aerodynamic characteristics of flying fish in gliding flight. *J. Exp. Biol.* **213**, 3269-3279.

Radespiel, R., Windte, J. & Scholz, U. 2006 Numerical and experimental flow analysis of moving airfoils with laminar separation bubbles. *AIAA Paper* 2006-501.

Selig, M. S., Donovan, J. F. & Fraser, D. B. 1989 *Airfoils at Low Speeds.* SoarTech.

Selig, M. S., Guglielmo, J. J., Broeren, A. P. & Giguére, P. 1995 *Summary of Low-Speed Airfoil Data.* Vol. 1. SoarTech.

Shyy, W., Lian, Y., Tang, J., Viieru, D. & Liu, H. 2007 *Aerodynamics of Low Reynolds Number Flyers.* Cambridge University Press.

Zhou, Y. & Wang, Z. J. 2012 Effects of surface roughness on separated and transitional flows over a wing. *AIAA J.* **50**, 593–609.

Zverkov, I., Zanin, B. & Kozlov, V. 2008 Disturbances growth in boundary layers on classical and wavy surface wings. *AIAA J.* **46**, 3149–3158.

종방향 스트립이 낮은 레이놀즈 수 익형에 미치는 영향

서울대학교 대학원
기계항공공학부
정민욱

요 약

본 연구에서는 종방향의 스트립이 이차원 SD7003 익형의 공력에 미치는 영향에 대해 조사하였다. 익형의 시위길이에 기반한 레이놀즈 수 0.6×10^5과 1.0×10^5에서 풍동 실험을 수행하였다. 종방향 스트립의 폭과 높이, 스트립 간의 너비를 조정해가면서 양력과 항력을 측정하였으며, 익형의 표면 근처에서 유동장도 분석하였다. 종방향의 스트립은 실속 받음각을 약 3도 정도 지연시키는 효과가 있었으며, 이로 인하여 실속 받음각 근처에서 양력이 증가하고 항력이 감소하였다. 이로 인하여 양항비가 상당히 증가하였다. 실속 받음각 근처인 11.4도에서 속도장을 측정한 결과, 날개의 전연에서 발생하는 유동방향 와류로 인하여 유동이 재부착되어 실속이 지연됨을 확인하였다.

주요어: 종방향 스트립, 익형, 실속, 양항비, 재부착, 유동방향 와류
학번: 2011-24069